Circulation and variability in the Chile Basin

Gary Shaffer[a,b,]*, Samuel Hormazabal[b], Oscar Pizarro[c], Marcel Ramos[d]

[a] *Department of Geophysics, Danish Center for Earth System Science, University of Copenhagen, Juliane Maries Vej 30, 2100 Copenhagen OE, Denmark*
[b] *Departamento de Física de la Atmósfera y del Océano, Programa Regional de Oceanografica Fisica y Clima, Universidad de Concepción, Concepción, Chile*
[c] *Departamento de Física de la Atmósfera y del Océano, Programa Regional de Oceanografica Fisica y Clima, Centro de Investigación Oceanográfica COPAS, Universidad de Concepción, Concepción, Chile*
[d] *Departamento de Oceanografía, Programa Regional de Oceanografica Fisica y Clima, Centro de Investigación Oceanográfica COPAS, Universidad de Concepción, Concepción, Chile*

Abstract

Current observations at several depths between 250 and 3750 m are reported from a 30°S, deep sea site 150 km off the Chile coast for the period July 1993–June 2001. These results are used with current observations from a nearby slope site, satellite altimeter data, and hydrographic and Acoustic Doppler Current Profiler data from the WOCE P6E section along 32.5°S to address mean and variable flow in the Chile Basin. Strong current variability in the upper ocean for periods more than 100 days is explained in terms of remotely forced Rossby waves, local baroclinic instabilities of coastal currents and variable wind forcing. Intraseasonal to seasonal current variability at the deep ocean site was greatest during La Niña events while intraseasonal variability at the slope site was greatest during the 1997–1998 El Niño event. Mean westward and poleward flow was observed at all depths at the deep sea site but upper ocean means were not significantly different from zero. There was a well-defined, mean poleward flow of $0.6 \pm 0.3\,\mathrm{cm\,s^{-1}}$ at 2450 m depth there. Geostrophic current calculations are presented for the P6E section with levels of no motion based on our current observations and other constraints. These reference choices yield reasonable and consistent results for the steady-state heat balance of the deep Chile and Peru Basins. Results show a deep equatorward flow of 3–4 Sv on the eastern flank of the East Pacific Rise and a deep poleward boundary flow of about 10 Sv within 1500 km of the Chile coast. Up to half of the total mid-depth outflow of the South Pacific may take place east of the Rise. Thus the deep poleward boundary current off Chile is a major component of the deep circulation of the global ocean but the dynamics of this current remain a puzzle.

*Corresponding author. Tel.: +46-35-32-06-12; fax: 45-35-32-05-76.
  E-mail address: gs@dcess.ku.dk (G. Shaffer).

1. Introduction

Until recently, direct observations of currents were lacking in the eastern South Pacific and our understanding of circulation there rested upon inferences from tracer distributions and on geostrophic calculations based on sparse hydrographic data (cf. Reid, 1986). The first reported recording current observations in the eastern boundary current system off Chile, limited to a 4–6 month period in 1991–1992, were obtained from depths of 100 and 3400 m at a 4200 m deep site 150 km off the coast at 30°S (Shaffer et al., 1995). In combination with local geostrophic current profiles from this period, these results were used to estimate a mean alongshore current profile at this site during this period. This profile featured poleward flow of about 2–3 cm s^{-1} in the 100–400 m depth range as well as deep poleward flow of about 1 cm s^{-1} below 1700 m.

In subsequent work, data was analyzed from a second current meter mooring at 30°S located over the slope at 850 m depth only 10 km off the coast. Current variability at this site is dominated by free, 40–70 day period, coastal trapped waves, ultimately forced by wind fluctuations in the equatorial Pacific associated with the Madden–Julian oscillation (Shaffer et al., 1997, 1999; Hormazabal et al., 2002). No expression of these waves was observed at the deep sea site, consistent with theoretical expectations that such waves would be trapped within 100 km of the coast off central Chile. Mean poleward flow of about 13 cm s^{-1} was observed over the slope in the core of the Peru–Chile Undercurrent (220 m depth). This flow exhibited strong semi-annual and weaker annual variations; poleward flow was strongest in the austral spring and fall and weakest in the winter. Interannual variability was also observed in the Undercurrent (Shaffer et al., 1999) and has been modeled with some success using a linear, frictional model forced by observed, El Niño/La Niña sea level changes at the equator (Pizarro et al., 2001) and with a simpler, frictionless model forced by observed winds along the equator in the Pacific Ocean (Pizarro et al., 2002). These results show that large phase lags found between local sea level and alongshore flow, both in the observations and in the model results, can be explained by Rossby waves propagating westward from the Chile coast.

Here, we return to consider currents throughout the water column at our deep sea site based on much more extensive moored current observations collected during an 8 year period from July 1993 to June 2001. With these results, our slope site data, satellite altimeter data and hydrographic and Acoustic Doppler Current Profiler (ADCP) data from the WOCE P6E line, we address the nature and the zonal distribution of intraseasonal, seasonal and interannual variability in the Chile Basin. We present mean flow results and use these results and additional constraints to reference geostrophic current calculations from the P6E line data between the Chile coast and the East Pacific Rise. We then test the results of these calculations by considering the steady-state heat balance of the deep Chile and Peru Basins. This procedure leads to an improved picture of north–south flow and transports in the subtropical, eastern South Pacific. Finally, we discuss our results in the light of other relevant observational and modeling studies.

2. Observations and methods

Between July 22, 1993 and June 11, 2001, a recording current meter (RCM) mooring was maintained at a deep ocean site about 150 km off the Chile coast and about 70 km seaward of the axis of the Peru–Chile trench (Fig. 1). This position (29°59'S, 73°11'W), essentially the same as occupied by our initial mooring in 1991–1992, is located at a depth of about 4300 m in a region of low abyssal hills (about 100 m height) at the eastern edge of the Chile Basin. The mooring was recovered and redeployed about twice yearly leading to the 14 observation periods listed in Table 1.

There were gaps of up to 3 months between periods 1 and 2, 2 and 3, 4 and 5, 5 and 6 and 10 and 11 (Table 1); otherwise the mooring was redeployed within a day or two after recovery. During periods 1–3, the mooring had four Aanderaa RCM 7 current meters. From period 4 onwards, five RCMs were used with nominal
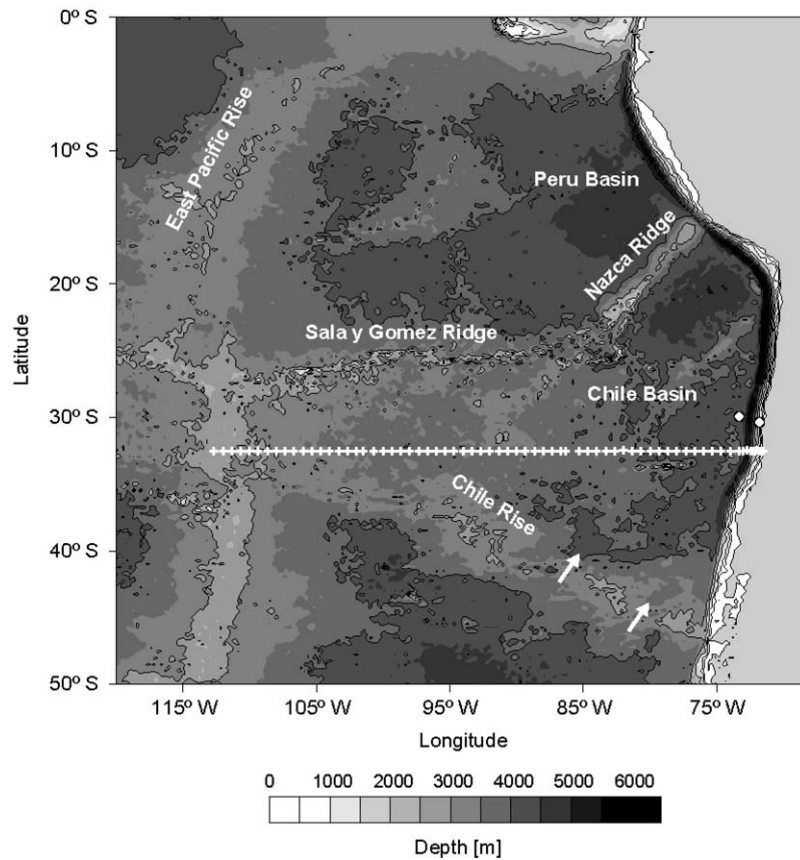
Fig. 1. Bathymetry of the eastern South Pacific Ocean. Also shown are the positions of the deep sea and slope current meter moorings near 30°S off Chile (white dots) and the station positions from the World Ocean Circulation Experiment (WOCE) P6E line occupied during May 1992 at 32.5°S (white crosses). The white arrows mark sites of deep inflow across the Chile Rise to the Chile Basin.

Table 1
Observation periods for the deep sea mooring

Observation period	Duration	Observation period	Duration
1	1993/07/22–1993/12/22	8	1997/02/12–1997/11/02
2	1994/01/25–1994/08/11	9	1997/11/03–1998/07/26
3	1994/09/25–1995/01/24	10	1998/07/27–1999/02/10
4	1995/01/27–1995/03/04	11	1999/02/11–1999/10/02
5	1995/06/06–1996/01/14	12	1999/10/03–2000/03/04
6	1996/01/26–1996/07/19	13	2000/03/05–2000/09/13
7	1996/07/20–1997/02/11	14	2000/09/14–2001/06/11

depths of 250, 450, 1350, 2450 and 3750 m (however, RCMs were only deployed at 250 m and 450 m depths during period 8). The deepest RCM was located 550 m over the bottom. Data recovery was about 50% from 1993 to 1995 but increased to over 80% from 1996 to 2001. All RCM's had speed, direction and temperature sensors. No attempt was made to correct the data

for "knockdown" but our simulations of mooring motion with our mooring design and observed currents indicated maximum "knockdown" of no more than 100 m for the upper two RCMs and considerably less than this for the lower three RCMs. Current speeds with zero rotor rotation (nominal speed of $1.1 \, \text{cm s}^{-1}$) were replaced by $0.55 \, \text{cm s}^{-1}$ while retaining measured direction. Regular rotation of current direction through tidal cycles always occurred at stall speeds. The original hourly RCM current data was low passed filtered with a 181-point Cosine–Lanczos filter with half amplitude point at 60 h. Three month running means were applied twice to this data to suppress intraseasonal variability. All time series treated this way are referred to below as low low passed.

Sea surface height (SSH) anomalies are based on combined processing of ERS 1,2 and TOPEX/ POSEIDON satellite data from AVISO. The anomalies are relative to mean sea levels for January 1993–January 1996 and correspond to grid data of $0.25 \times 0.25°$ resolution every 10 days from March 1995 to December 2000. Weekly averaged, sea surface wind stress data from ERS satellite scatterometer observations between July 1993 and July 1999 were obtained from D-épartement d'Océanographie Spatiale, IFRE-MER. Daily mean, sea surface wind stress data from QuikSCAT satellite scatterometer observations between July 1999 and June 2001 were obtained from the Jet Propulsion Laboratory. Data from the WOCE P6 hydrographic line at $32.5°S$ from the South American coast to the East Pacific Rise ($112°W$) were obtained from WOCE Hydrographic Program Office. Absolute current velocity data from shipboard ADCP along this line were obtained as hourly means centered at 10 m depth intervals from the Joint Archive for Shipboard ADCP at the University of Hawaii.

3. Moored current results

The rotary spectra of kinetic energy density for the current meters on the deep sea mooring show diurnal and semi-diurnal fluctuations which decrease with depth as well as spectral peaks—sharpest near the ocean bottom—at periods of 8 and 6 h (Fig. 2). These results confirm and improve upon earlier results based on much shorter records at this site (Shaffer et al., 1995). For periods of 1 day and less, anticlockwise rotation dominates in the upper ocean. Near the bottom, there is about equal power in both rotation senses indicating alternating currents. These results can be interpreted in terms of (1) strong inertial oscillations (1-day period and anticlockwise rotation at $30°S$) superimposed upon the barotropic diurnal tide, (2) the semidiurnal tide and (3) leakage of energy from the inertial oscillations and/or the tides to higher harmonics. Inspection and wavelet analysis of these time series (not shown) show bursts of inertial oscillations that occur earlier near the surface and later at depth. The deep observations may be capturing remnants of oscillations generated earlier in the surface layer 200–300 km farther to the south (Garrett, 2001). Thus, apparent vertical phase lags of these bursts at the mooring site may reflect the generation of inertial oscillations by wind events of large horizontal extent. Also, at our $30°S$ site, inertial oscillations may be resonantly forced by the diurnal tide or the sea breeze cycle (Shaffer, 1972). An in-depth analysis of these features and possibilities is beyond the scope of the present paper but is the subject of other work in progress.

At longer periods, results for all four current meters show clockwise and anti-clockwise energy increasing in tandem with increasing period, whereby the largest relative increases are found in the upper layers with the spectral slope approaching -2 at 250 m depth compared to about -1.5 at 3750 m depth. There is no indication of increased variability at the 50–60 day period in these long records, confirming that the strong variability of these periods observed at the slope mooring (Shaffer et al., 1999) is trapped over the shelf and slope. At all depths this increase breaks off with a peak in energy at a period of about 120 days. At longer periods in the upper ocean, anti-clockwise energy falls off leaving clockwise rotation to dominate. This is not seen at the deep current meters where the currents remain essentially alternating, and presumably topographically guided, at all frequencies.
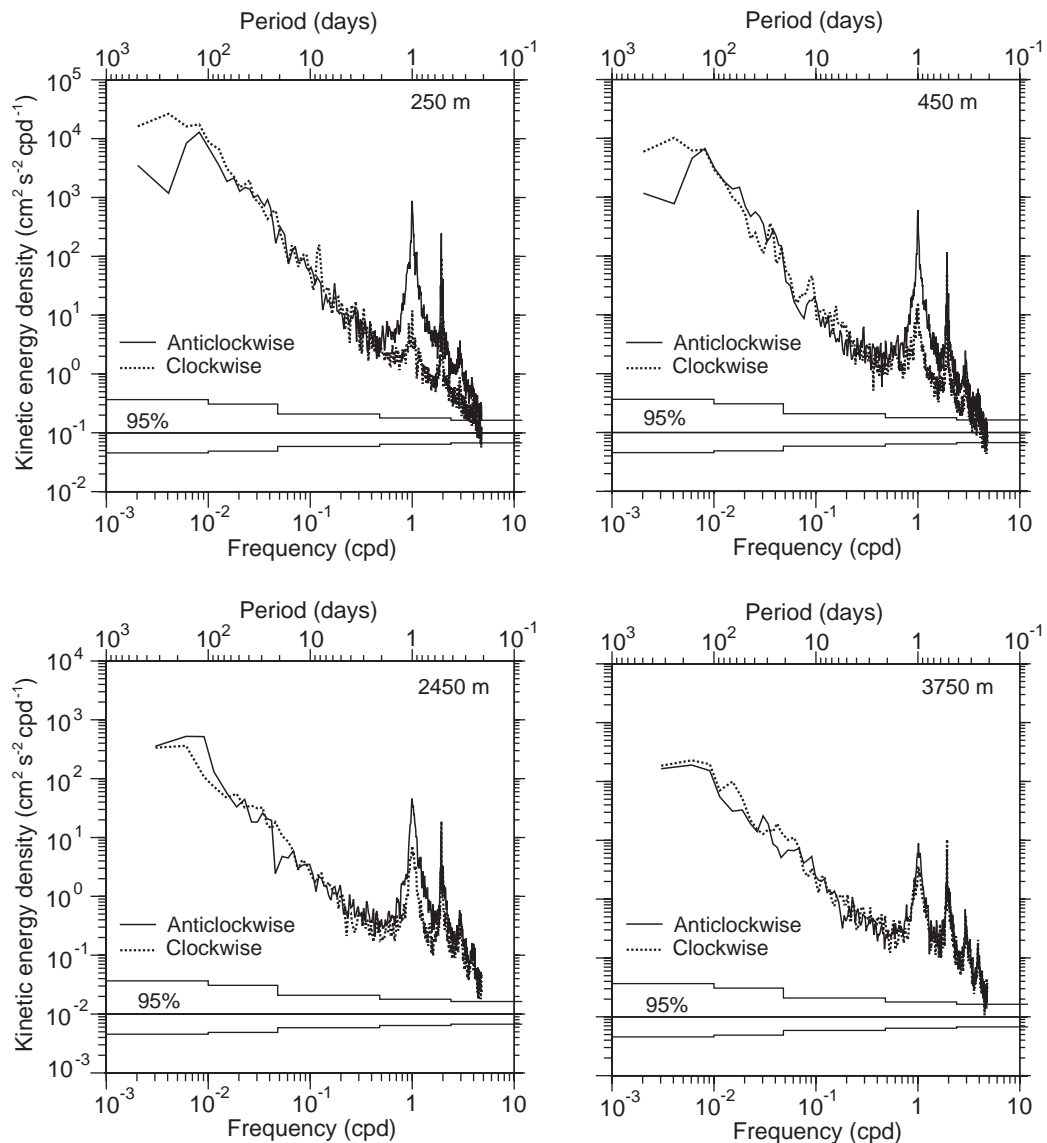
Fig. 2. Clockwise and counterclockwise spectra of kinetic energy density for current meter records from the nominal depths of 250, 450, 2450, and 3750 m at the deep sea mooring off Chile (left white dot in Fig. 1). Spectral calculations were made with 8, 10, 20, 30, and 40 degrees of freedom for the frequency ranges 10^{-3}–10^{-2} cycles per day (cpd), 10^{-2}–2×10^{-3} cpd, 2×10^{-3}–2×10^{-2} cpd, 2×10^{-2}–10^{-1} cpd, and 10^{-1}–0.5 cpd, respectively. The calculations were based on the periods January 1996–June 2001 (250 and 450 m depths) and November 1997–June 2001 (2450 and 3750 m depths).

The complex nature of low-frequency variability at our deep ocean site can be appreciated in Fig. 3, a presentation of all low-passed current data there over our 8-year mooring period. One striking feature of these results is interannual modulation of the nature of the current variability in the upper ocean. This variability is generally strong and exhibits clockwise rotation during La Niña conditions in 1995–1996 and 2000–2001. During the 1997–1998 El Niño event, variability is generally weaker and exhibits anti-clockwise rotation (however one very strong, anti-clockwise signal was
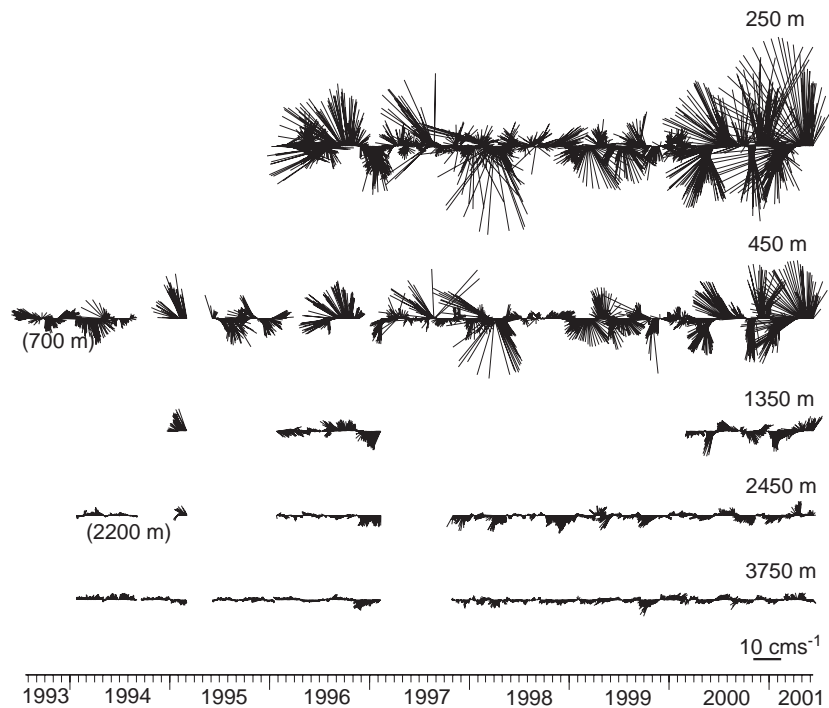
Fig. 3. Low passed time series of vector current (north upward) observed at the nominal depths of 250, 450, 1350, 2450, and 3750 m at the deep sea mooring over the 1993–2001 study period. Original hourly data were low pass filtered with a 181 point Cosine–Lanczos filter with a half amplitude point at 60 h and plotted as daily averages. The current scale is indicated in the lower right hand corner and deviating observation depths are given below corresponding time series.

observed during the first half of 1998). Many of the fluctuations in the upper ocean can be traced visually to the deep ocean at this site. There are some in phase and some out of phase connections between upper and deep ocean, perhaps reflecting partition of energy between different vertical modes.

For the low-pass current records at our deep ocean site (Fig. 3), we calculated means, standard deviations, integral time scales and standard errors of the east–west (u) and north–south (v) components as well as kinetic energies for each observation period with available data and for total record lengths (Table 2). An estimate for the 95% confidence interval for the calculated means is given by $M \pm t$SE where M is the mean, SE is the standard error and t is a multiplier that depends upon the degrees of freedom, N, of the low-passed time series, as estimated from the series record length divided by twice the integral time scale. For our results, N was > 5 for the individual observa-

tion periods and > 50 for the overall means, leading to a $t < 2.6$ for the individual periods and a t of about 2 for the overall means. Weak mean poleward flow was observed over the whole water column but, in the presence of strong variability in the upper layers, such flow was only different from zero to the 95% confidence level at the depth of 2450 m with an overall mean speed of $0.6 \pm 0.3 \, \text{cm s}^{-1}$. However at this depth and at 3750 m depth, there was considerable long-term flow variability including northward flow during 1993/1994 (observation periods 2 and 3). The deep, mean poleward flow will be discussed at length below. Likewise, weak mean westward flow was observed throughout the water column but, in the presence of strong variability in the upper layers, such flow was only different from zero at the 95% confidence level at depths of 450, 2450 and 3750 m with overall mean speeds of 1.3 ± 0.9, 0.9 ± 0.3 and $0.3 \pm 0.2 \, \text{cm s}^{-1}$, respectively.

Table 2
Statistics of low passed current records from the deep sea mooring

Observation Period	BLD (%)	$M\,u$ (cm s^{-1})	$M\,v$ (cm s^{-1})	SD u (cm s^{-1})	SD v (cm s^{-1})	IT u (day)	IT v (day)	SE u (cm s^{-1})	SE v (cm s^{-1})	$|V|_{\max}$ (cm s^{-1})	K_{e} (cm^2 s^{-2})
250 m											
6	1.3	6.2	1.2	8.3	4.8	16	13	3.6	1.9	23.9	45.6
7	1.5	−2.7	−0.1	9.7	11.5	12	22	3.2	5.3	30.0	112.6
8	4.8	−3.4	0.4	5.7	7.2	10	8	1.6	1.8	31.1	41.6
9	6.9	−1.2	−2.3	8.4	8.4	7	6	1.9	1.8	36.1	70.6
10	5.4	3.5	−0.2	4.9	4.1	12	9	1.7	1.2	16.2	20.6
11	6.3	−0.1	−2.0	6.2	6.8	10	12	1.8	2.2	21.9	42.6
12	6.4	−0.5	0.1	4.7	4.8	9	7	1.7	1.4	15.6	22.7
13	5.4	−7.5	−2.9	8.4	12.7	14	19	3.2	5.6	29.4	115.7
14	0.0	−4.0	3.5	11.6	18.2	11	13	3.3	5.7	46.5	233.0
Total mean	4.2	−1.3	−0.2	8.8	10.3	—	—	0.9	1.1	46.5	92.1
450 m											
1	15.8	−0.2	0.2	4.5	2.6	5	13	1.2	1.1	9.6	13.6
2	38.7	0.9	−2.7	2.3	3.4	5	12	0.5	1.2	10.9	8.6
4	2.8	−5.8	9.8	2.5	4.2	—	—	—	—	19.5	11.7
5	12.8	1.4	−1.5	4.3	4.4	16	11	1.7	1.4	13.8	18.8
7	11.7	−4.4	3.9	5.3	6.2	11	12	2.3	2.8	16.4	33.3
8	23.0	−2.1	−0.3	4.8	4.4	8	8	1.2	1.1	30.2	21.5
9	22.0	−1.2	−1.7	5.9	6.2	8	8	1.5	1.5	28.1	36.6
10	23.0	1.4	−0.4	2.9	2.7	16	14	1.2	1.0	8.7	8.0
11	14.7	0.6	−1.1	4.3	5.6	9	12	1.2	1.8	13.3	25.0
12	21.2	−0.7	−0.6	3.8	4.1	7	5	1.2	1.1	24.4	15.7
13	7.7	−5.8	−1.4	4.7	8.0	15	20	1.8	3.7	18.6	43.0
14	2.7	−3.7	1.0	6.8	11.0	12	14	2.0	3.6	24.7	83.9
Total mean	17.2	−1.3	−0.4	5.3	6.4	—	—	0.5	0.6	30.2	34.3
1350 m											
4	1.9	−3.6	4.8	0.9	2.4	—	—	—	—	9.8	3.4
6	48.5	1.5	−0.4	1.8	0.9	6	2	0.5	0.1	6.7	2.0
7	32.4	−1.1	−0.6	1.8	3.4	12	20	0.6	1.5	7.7	7.5
13	34.9	−1.4	−0.8	1.7	2.6	9	13	0.5	1.0	10.7	4.9
14	11.2	−0.2	−0.7	2.8	3.0	13	15	0.9	1.0	8.9	8.5
Total mean	28.4	−0.5	−0.4	2.4	2.9	—	—	0.4	0.4	10.7	7.3
2450 m											
2	78.3	−0.1	0.5	0.4	0.7	6	8	0.1	0.2	3.4	0.4
4	56.0	−1.6	1.2	1.3	1.5	—	—	—	—	5.1	1.9
6	67.6	−0.1	−0.1	1.3	0.6	6	7	0.3	0.2	3.5	1.0
7	58.5	−0.6	−1.6	0.9	1.5	8	12	0.3	0.5	5.2	1.5
9	52.9	−1.0	−1.3	1.2	1.5	12	11	0.4	0.4	6.8	1.9
10	48.3	−0.7	−1.9	0.8	2.0	4	14	0.2	0.8	7.5	2.5
11	49.8	−1.3	−0.2	1.4	1.6	9	9	0.4	0.4	7.2	2.3
12	47.0	−0.9	−1.0	2.2	1.7	9	8	0.8	0.6	7.3	3.9
13	50.0	−1.4	0.3	1.4	1.1	10	11	0.5	0.4	6.1	1.6
14	34.9	−1.1	−0.6	1.4	1.8	14	10	0.5	0.5	6.0	2.7
Total mean	53.8	−0.8	−0.6	1.4	1.7	—	—	0.1	0.2	7.5	2.4

Table 2 (continued)

Observation Period	BLD (%)	$M\,u$ (cm s^{-1})	$M\,v$ (cm s^{-1})	SD u (cm s^{-1})	SD v (cm s^{-1})	IT u (day)	IT v (day)	SE u (cm s^{-1})	SE v (cm s^{-1})	$|V|_{\max}$ (cm s^{-1})	K_e (cm^2 s^{-2})
3750 m											
2	74.4	0.1	1.0	0.4	0.6	6	6	0.1	0.2	2.8	0.3
3	87.3	−0.1	0.3	0.5	0.4	9	6	0.2	0.1	1.9	0.2
4	67.2	0.3	−1.1	0.3	0.4	—	—	—	—	2.4	0.2
5	83.6	−0.5	0.1	0.8	0.4	6	6	0.2	0.1	4.1	0.4
6	81.8	−0.4	0.1	0.5	0.5	6	11	0.1	0.2	2.0	0.3
7	62.0	−0.6	−0.8	1.3	1.6	7	13	0.3	0.6	6.0	2.1
9	73.1	−0.3	−0.7	0.7	0.9	11	6	0.2	0.2	3.5	0.7
10	73.0	−0.4	−0.6	0.6	0.6	4	11	0.1	0.2	2.8	0.4
11	63.7	−0.4	−0.3	1.2	0.7	12	5	0.4	0.1	4.7	1.0
12	41.9	0.4	−0.3	1.9	1.8	10	12	0.7	0.7	7.8	3.4
13	59.9	−0.6	0.0	1.0	1.1	10	10	0.3	0.4	5.7	1.2
14	55.5	−0.3	0.1	1.2	1.0	15	11	0.4	0.3	3.6	1.3
Total mean	68.3	−0.3	−0.1	1.0	1.1	—	—	0.1	0.1	7.8	1.2

Original hourly data were low pass filtered with a 181 point Cosine-Lanczos filter with a half amplitude point at 60 h. Observation periods are given in Table 1. BLD is the percentage of observations below 1.1 cm s^{-1}, the limit of detection of the current meters. Velocity components u and v are directed toward 90° and 0°, respectively. M, SD, IT and SE denote mean, standard deviation, integral timescale and standard error for u and v. $|V|_{\max}$ is the maximum speed observed in the low passed (LP) records. The eddy kinetic energy K_e, is half the sum of the variances of LP u and v. Also included are total study period means at each depth of the above properties. IT and SE were not considered for (short) observation period 4. The IT's were calculated from the detrended, LP time series as the discrete integral of the time-lagged autocorrelation function from zero lag to the first zero crossing. For each period and depth, SE's were calculated as SD/$\sqrt{N}$ where N is the number of degrees of freedom obtained by dividing period record lengths by twice the period IT's. For the total study period at each depth, SE's were calculated using the sum of individual period N's at each depth.

Results for eddy kinetic energy confirm the impression of Fig. 3 of strong interannual variability with greatest variance in the upper ocean during La Niña conditions (for example, observation periods 7, 13 and 14). In contrast, greatest eddy kinetic energy was found during El Niño events at our slope site, reflecting greater coastal trapped wave activity (wave periods of 70 days or less) during such events (Shaffer et al., 1999). Low pass variability at our deep ocean site is dominated by periods of 100 days or more and reflects other processes as discussed below. Low low passed currents at our deep sea mooring site and local winds exhibit a mixture of seasonal and inter-annual variability (Fig. 4). Harmonic analysis shows that annual fluctuations dominate the seasonal-scale, current variability at the upper two current meters as well as the seasonal-scale, alongshore wind stress variability (Table 3). In contrast to the observations at the deep sea site, semi-annual current variations were found to dominate at our slope mooring (Shaffer et al.,

1999). Recent work suggests that these coastally amplified, semi-annual fluctuations are remotely forced by semi-annual, wind fluctuations in the equatorial Pacific and reach the study area by way of equatorial and coastal wave guides (Pizarro et al., 2002).

During 1993–1995, the seasonal cycle of along-shore winds was quite weak. This was followed by an enhanced, phase-shifted seasonal cycle from mid-1996 to the end of the 1997–1998 El Niño event and a more regular seasonal cycle throughout the rest of the study period. Strong local wind anomalies during the latter half of 1996, also associated with wind stress curl anomalies (Shaffer et al., 1999), may have contributed to the forcing of strong current anomalies at the deep ocean site during this period (Fig. 4). However, the return of strong current anomalies during 2000–2001 was not associated with anomalous local winds. There is no clear interannual modulation of upper ocean flow at our deep sea site. In particular, mean flow there during the strong 1997–1998 El Niño event
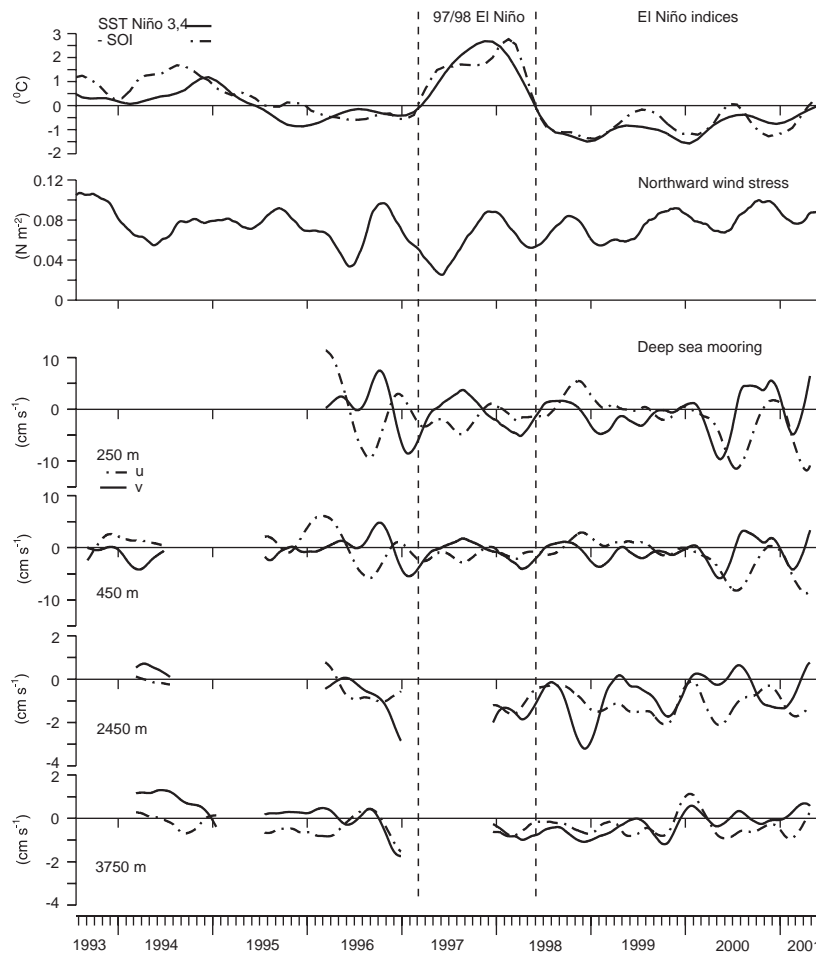
Fig. 4. Low low passed (twice filtered with a 3 month running means) anomalies of sea surface temperature for the Niño 3,4 region (5°N–5°S, 120°W–170°W) and the 1991–1997 period (SST Niño 3,4), low low passed Southern Oscillation Index (SOI) multiplied by −1, low low passed northward wind stress from weekly averaged, ERS1,2 and QuikSCAT satellite winds from a 1 × 1° square, centered at 30.5°S–73.5°W, close to moorings, and low low passed time series of *u* (east–west) and *v* (north–south) current components observed at 250, 450, 2450, and 3750 m depths at the deep sea mooring. Original hourly data were low pass filtered and daily averaged as for Fig. 3 and then low low passed. The dashed vertical lines bracket the El Niño 1997–1998 period, bounded by zero SOI values. Only the northward wind component is shown since it represents well wind stress in the local alongshore direction, the dominant wind direction for the low low passed winds in the region.

appears no different than before or after the event although weaker interannual changes may be masked by strong observed seasonal-scale variability (Fig. 4). On the other hand, there is an indication of increased southward flow in the deep ocean at this site during and after this El Niño event (although there was a large data gap below 450 m during most of 1997; Fig. 4). Maximum southward flow in the Peru–Chile Undercurrent at

our slope station was found to lead the 1997–1998 El Niño event by about 9 months, a phasing consistent with the local seaward propagation of this event as a Rossby wave (Pizarro et al., 2002). Presumably, this Rossby wave subsequently passed by our deep sea mooring site. Indeed, in-depth analysis of current meter observations from our slope and deep sea moorings confirms the westward passage of seasonal and interannual

Table 3
Amplitude, phase and % variance explained for annual and semiannual harmonics of low low pass current and wind stress

	Annual			Semiannual		
	Amplitude	Phase	% Variance	Amplitude	Phase	% Variance
u component						
Wind stress	0.25	314.1	45.1	0.06	352.9	2.6
250 m	3.0	336.1	41.3	1.0	280.2	4.8
450 m	1.7	335.4	25.0	0.9	289.5	7.4
2450 m	0.2	289.6	9.8	0.1	19.2	1.9
3750 m	0.2	15.8	7.8	0.1	47.3	1.2
v component						
Wind stress	1.3	302.6	69.8	0.21	161.6	1.8
250 m	3.0	283.4	42.1	0.3	136.0	0.4
450 m	1.7	272.8	38.8	0.3	120.6	1.4
2450 m	0.8	158.4	52.7	0.4	95.7	11.4
3750 m	0.2	126.2	19.6	0.2	49.4	19.5

Values calculated for the period December 12, 1997 to April 26, 20001. Amplitude is in 10^{-2} N m^{-2} for wind stress and cm s^{-1} for currents. Phase is in number of days after January 1. % Variance explained is for the combined seasonal–interannual band. Low low passed wind stress records are derived from weekly mean values from ERS-1,2 and daily Quickscat satellite wind data at a $1 \times 1°$ square centered on 30.5°S and 72.5°W between the slope and deep sea moorings.

scale Rossby waves through this site with phase speeds of 2–3 cm s^{-1} (Hormazabal et al., 2004). Most interannual variability of SSH anomalies between the coast and about 90°W may be forced by remotely forced Rossby waves emanating from the coast (Vega et al., 2003).

Additional observations and analyses from the Chile Basin aid in interpreting the nature and distribution of the strong, low-frequency variability observed at our deep sea mooring site. Fig. 5 (top) shows the distribution of low passed SSH anomalies along 30°S on a line between the Chile coast and the East Pacific Rise, as calculated from combined TOPEX/POSEIDON and ERS 1,2 altimetry data for period 1995–2000. Results show enhanced SSH anomaly variance between the coast of Chile and about 82°W. Our deep sea mooring is situated near the maximum of this enhanced variance that defines a coastal transition zone off Chile (Hormazabal et al., 2004). Recent, high-resolution, numerical simulations of currents off Chile exhibit a zone of about the same width, populated by meanders and eddies with horizontal scales of about 150 km (Leth and Shaffer, 2001). The model eddies are formed by baroclinic instability of the coastal current system. Thus,

the energetic and complex current variability observed in the upper ocean at our deep sea site likely reflects a combination of remotely forced Rossby waves and locally generated eddies and meanders passing by the mooring.

A complimentary view of the low-frequency variability in the Chile Basin is provided by upper ocean currents observed from shipboard ADCP and calculated from geostrophy along the WOCE P6E line at 32.5°S between the coast of Chile and the East Pacific Rise (Fig. 5, bottom). The good agreement between observed and calculated currents shows that low-frequency motions dominated current fluctuations along this line at this time and that the hydrographic station spacing employed across this line was generally fine enough to resolve these motions. In the eastern part of this section, within the zone of large intraseasonal and seasonal SSH anomalies, current structures exhibit horizontal scales of about 200 km, not unlike the scales of the baroclinic eddies in the numerical simulations. Quasi-geostrophic current variability tends to be weaker within the central Chile Basin (around 90°W). As the eastern slope of the East Pacific Rise is approached, large-amplitude features appear with
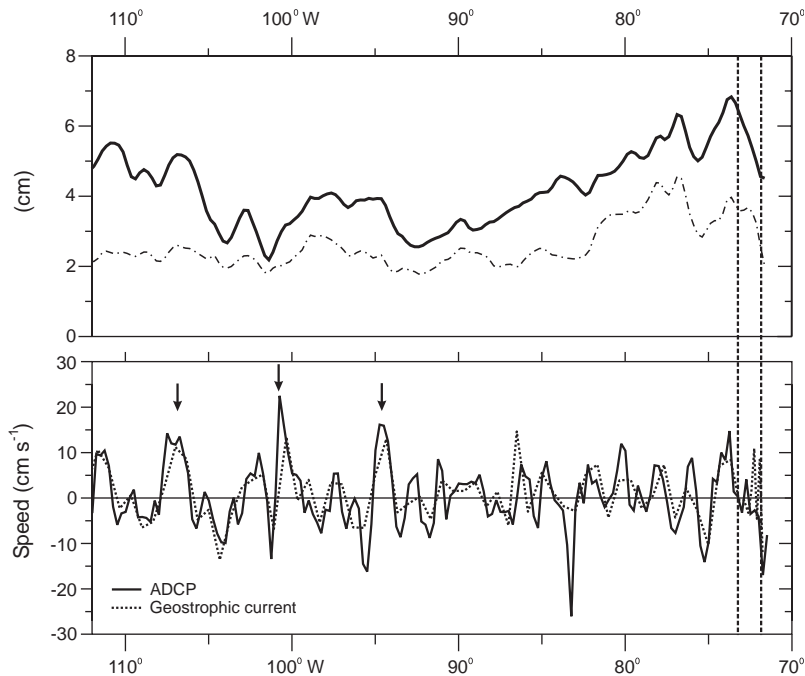
Fig. 5. (Top panel): Total (thick line) and high pass (periods less than 180 days; thin dashed line), root-mean-square, sea surface height (SSH) anomalies along 30°S from the coast of Chile to the East Pacific Rise for the period April 1995–December 2000, based on merged TOPEX/POSEIDON and ERS-1,2 satellite data of SSH anomaly with 0.25° × 0.25° and 10 day resolution. The dotted vertical lines mark the seaward positions of the slope and deep sea moorings. (Bottom panel): Northward velocity at 150 m depth along the WOCE P6E line at 32.5°S from shipboard Acoustic Doppler Current Profiler, averaged zonally over 0.25° (solid line), and from geostrophic calculations, based on the P6E line hydrographic data, and plotted at positions between station pairs (dotted line). Geostrophic calculations were referenced to levels of no motion chosen below (and shown in Fig. 6) but any choice below, say, 3000 m would yield about the same results at 150 m depth. The arrows mark large-amplitude, current anomalies in the western Chile Basin with about 600 km separation.

about 600 km east–west scales. Such features and the observed increase in seasonal SSH variance in this region (Fig. 5, top) may reflect first mode, Rossby waves of annual period which propagate slower and "pile up" as the East Pacific Rise is approached, perhaps in response to shallower water depth and/or eastward mean flow in this region. Simple model results suggest the dominance of wind-forced, Rossby waves west of 90°W (Vega et al., 2003).

4. Mean circulation in the Chile Basin

Long-term current observations from our deep ocean site at 30°S showed highly variable flow in the upper ocean, mean southward flow of

$0.6 \pm 0.3 \, \text{cm s}^{-1}$ at 2450 m depth, and flow approaching zero at 3750 depth, $0.1 \pm 0.2 \, \text{cm s}^{-1}$ to the south. There was considerable interannual variability in the southward flow at the latter two depths. This shows that long records such as ours are necessary for defining the mean flow in the study region and that care is needed in interpreting geostrophic current calculations from one-time hydrographic surveys in this region. Here, we use our mean flow results, together with other constraints developed below, to reference such calculations based on the WOCE P6E line hydrographic data. In recent work, three different groups have carried out such calculations based on data from this section, using different approaches to reference these calculations (Tsimplis et al., 1998; Wijffels et al., 2001; Sloyan and

Rintoul, 2001). In Part 5, we discuss our results below in the light of this and other work on the mean circulation of the subtropical, eastern South Pacific Ocean.

For our geostrophic transport calculations we choose to divide the WOCE P6E line into four sections based on the observed density distribution and the characteristics of the variability considered above. The first section between the Chile coast and 76°W includes the nearshore zone of strong horizontal density gradients. The third section between 89°W and 102°W is characterized by flat density distributions at depth. The eastern edge of this section corresponds to a weak rise in bottom topography separating the deeper eastern part of the Chile Basin from its shallower western part (Fig. 1). The second and fourth sections (76–89°W and 102–112°W) exhibit moderate horizontal density gradients at depth. We find sections chosen in this way to be wide enough to avoid much of the possible influence of the current variability from Rossby waves and eddies on our transport calculations.

For these calculations we divided the P6E line vertically into six layers (Table 4). These layers were chosen based on the water mass properties of the region. Thus the second and third layers correspond to density ranges occupied by Equatorial Subsurface Water (of the Peru–Chile Undercurrent) and SubAntarctic Mode Water/Antarctic Intermediate Water (SAMW/AAIW), respectively. We identify the fourth and fifth layers with upper and lower Pacific Deep Water, respectively. The density surface dividing layers 5 and 6 is assumed to be a level of no motion. Our current observations, albeit from 280 km farther north, indicate that this surface should lie slightly below 3750 m depth at about 150 km off the coast (and 70 km seaward of the Peru–Chile Trench). On this basis we make a preliminary choice of the density level 45.83 (σ_4), corresponding to a potential temperature of 1.38°C, as the boundary between layers 5 and 6 and, thus, as our level of no motion from the coast to 89°W. This level is found at a pressure of about 3820 dbar at 150 km from the coast along the P6E line. With this choice of level of no motion we found a mean southward velocity of 0.6 cm s^{-1} in layer 5 of the section between the Chile coast and 76°W. This agrees well with our 8-year mean flow of 0.6 ± 0.3 cm s^{-1} observed at 2450 m depth, 150 km from the coast at 30°S.

There is another compelling reason to choose the level of no motion in the eastern Chile Basin along a deep density surface: The deep Chile and Peru Basins are filled by Circumpolar Deep Water from the south (Lonsdale, 1976) by way of several gaps in the eastern Chile Rise (arrows in Fig. 1). Thus, in the mean, there must be a deep level of no

Table 4
Layers boundaries, depths, potential temperatures, salinities, and transports for WOCE P6E section in the Chile Basin

Layer number	Layer boundary	Z_m (m)	θ_m (°C)	S_m	T_{WCB} (Sv)	T_{ECB} (Sv)
	Surface	0	18.88	34.83		
1					3.2	3.4
	26.0(σ_0)	183	12.78	34.45		
2					2.8	1.7
	26.9(σ_0)	417	7.14	34.37		
3					5.8	1.2
	36.5(σ_2)	1095	3.53	34.42		
4					1.1	−4.5
	36.9(σ_2)	2123	1.92	34.64		
5					2.4	−5.2
	45.83(σ_4)	3700	1.38	34.69		
6					—	0.5
	Sea floor	—	—	—		

Z_m, θ_m, and S_m are mean depths, potential temperatures and salinities on density or physical surfaces chosen for layer boundaries in the Chile Basin, as calculated from WOCE P6E line hydrographic data. T_{WCB} and T_{ECB} are the geostrophic transports calculated here for each layer in the western and eastern Chile Basin, respectively (west and east of 89°W).

motion there that separates the northward abyssal flow of this heavy water and the (observed) southward flow of lighter Pacific Deep Water. To test our choice for this level of no motion we consider heat conservation in the Chile and Peru Basins north of 32.5°S, bounded above by the 1.38°C potential temperature surface and below by the sea floor. In a steady state, heating of water within this volume, from above by (mainly) diapycnal diffusion across the upper surface and from below by geothermal heating at the sea floor, is balanced by cooling due to inflow of cooler water across 32.5°S below the upper surface, water which subsequently upwells through that surface with the (warmer) potential temperature of the surface. Such an approach is valid for long time scales and for potential temperature (density) surfaces below which only inflow from the south occurs.

To estimate the total (advective) cooling rate in the control volume, we calculate local geostrophic currents from the P6E hydrographic data below the 45.83 σ_4 surface (referenced by the assumed level of no motion on this surface), multiply these currents by the difference between local observed potential temperature and the 1.38°C reference, and sum the results over the (vertical) area between the reference surface and the sea floor along the P6E line. These calculations yield a total mean (northward) transport below the 1.38°C surface at 32.5°S of 0.46 Sv and a total mean cooling rate in the control volume of 1.12×10^{10} W. From available hydrographic data (mainly from WOCE lines along 88°W and 17°S) and bottom depth data, the area covered by the 1.38°C surface and the volume below this surface in the Chile and Peru Basins north of 32.5°S are about 1.2×10^{12} and 6.8×10^{14} m^3, respectively. From these estimates, the mean upwelling velocity across this surface in the Chile and Peru Basins north of 32.5°S is about 4×10^{-7} m s^{-1} and the residence time below this surface there is about 50 years. Likewise, the mean (advective) cooling rate per unit area below this surface there is about 9.4×10^{-2} W m^{-2}.

Based on a compilation and analysis of global heat flow data (Pollack et al., 1993), a conservative estimate of geothermal heat flux for the deep parts of the Chile and Peru Basin is about 5×10^{-2} W m^{-2}. Thus, for overall heat balance in our control volume, an additional, downward diffusive heat flux across the 1.38°C surface of about 4.4×10^{-2} W m^{-2} would be required. These estimates already suggest that geothermal heat flux may be as important as vertical diffusion in the heat balance and deep water renewal of the deep Chile and Peru Basins. The diffusive heat flux may be estimated as the product of a heat capacity, a diapycnal diffusion coefficient and a local vertical temperature gradient. Hydrographic observations in these basins (e.g. Tsuchiya and Talley, 1998) show a very weak, vertical temperature gradient at the 1.38°C surface (and, indeed, throughout the deep parts of these basins), decreasing from about 5×10^{-3}°C m^{-1} in the Chile Basin to about 1×10^{-4}°C m^{-1} in the Peru Basin. The estimates and observations above lead to a diapycnal diffusion coefficient estimate of about 0.5– 1.0×10^{-4} m^2 s^{-1}. In light of recent observational evidence (Polzin et al., 1997), this seems to be a reasonable value for the deep Chile and Peru Basins with moderate topographic "roughness" (see Fig. 1). Our values lie at the lower end of diffusion coefficient estimates for the deep Brazil Basin from heat balance and topographic roughness considerations ($1–5 \times 10^{-4}$ m^2 s^{-1}; Morris et al., 2001). This is consistent with less deep tidal dissipation (implying less deep mixing) in our study region than in the South Atlantic (Egbert and Ray, 2000), due to smoother bottom topography and weaker tides in our study region. Thus, our preliminary choice of the 45.83 σ_4 surface as a level of no motion leads to a reasonable and consistent picture for the heat balance and the abyssal mixing in the deep Chile and Peru Basins.

We also made similar calculations for a number of different density surfaces as assumed levels of no motion to test the sensitivity of heat balance, abyssal mixing and transports to these choices (Table 5). For only slightly larger reference densities, heat balance calculations lead to unrealistic, negative diffusion coefficients. This constraint puts a rather firm upper bound on appropriate density choices to define a level of no motion and, as a consequence, puts a rather firm upper bound of 10–12 Sv on the poleward

Table 5
Sensitivity of heat balance and transport calculations to choice of density surface as a level of no motion

σ_4 (kg m^{-3})	θ (°C)	$P(\theta)$(dbar)	$H(\theta)(10^{10}$ W)	$A(\theta)(10^{12}$ m^2)	$k(\theta)(10^{-4}$ m^2 s^{-1})	T_{DBC} (Sv)
45.82	1.430	3560	2.89	2.5	0.8–1.6	−7.3
45.83	1.383	3820	1.12	1.2	0.5–1.0	−9.7
45.84	1.335	3980	0.13	0.6	(<0)	−12.5

θ is a mean potential temperature along the WOCE P6E line on a chosen σ_4 surface. $P(\theta)$ is a pressure at which θ is observed at station 14 along this line at about the same seaward distance as for our deep sea mooring near 30°S. $H(\theta)$ is an (advective) cooling rate below a θ surface in the Peru and Chile Basins north of the P6E line and $A(\theta)$ is an area of this surface (see text). $k(\theta)$ is a mean diapycnal diffusion coefficient on this surface as estimated from mean heat balance with a mean geothermal heating of 5×10^{-2} W m^{-2} and a mean vertical temperature gradient on this surface of 5×10^{-3}–1×10^{-4}°C m^{-1} (see text). T_{DBC} is the transport below 36.5 σ_2 (see Table 4) in the deep poleward boundary current off Chile (east of 89°W), calculated from P6E hydrographic data with a chosen σ_4 surface as a level of no motion.

transport of Pacific Deep Water in the deep boundary current off Chile as estimated from P6E line hydrographic data (Table 5). For slightly smaller reference densities, heat balance calculations lead to somewhat larger, still reasonable diffusion coefficients. However, these reference choices lead to results that agree less well with our long-term current meter observations. For example, the choice of the 45.82 σ_4 surface leads to northward flow below 3560 dbar about 150 km offshore and a mean southward velocity of 0.4 cm s^{-1} in layer 5 of the section between the Chile coast and 76°W. Thus the 45.83 σ_4 surface appears to be the best choice for a level of no motion east of 89°W along 32.5°S.

The geostrophic calculations across the rest of the P6E line were made as follows: between 72.5°W and the Chile coast, we extrapolated dynamic heights relative to the level of no motion at 72.5°W using the height slope at the nearest two hydrographic profiles (Reid and Mantyla, 1976; an alternative choice in this zone of the sea floor as the level of no motion did not change our transport results below). Between 89°W and 104°W we chose the mean depth of the bottom, 3650 m, as the level of no motion: The Chile Rise and the Sala y Gomez Ridge run approximately parallel to the south and north of this section (Fig. 1) such that little meridional flow across this section would be expected below, say, 3000 m. Indeed, lack of horizontal density gradients (and geostrophic shear) at depth between 89°W and 104°W in the P6E data is consistent with this

expectation. Thus, any choice below about 3000 m of the level of no motion there would not change our transport results. Finally, between 104°W and 110°W and 110°W and 112°W we again chose the mean depth of the bottom, here 3300 and 2700 m, respectively, as levels of no motion. There is less a priori motivation for these choices but we found that reasonable variations about these levels, say ±200 m, did not change our transport results significantly.

Fig. 6 and Table 4 show the results of our geostrophic transport calculations from the P6E line hydrographic data and our level of no motion choices, for the horizontal sections and vertical levels chosen above. The main feature of our results is a deep, poleward flow of Pacific Deep Water within about 1500 km from the coast with a total transport of nearly 10 Sv. This flow is more diffuse in its shallower part and is more concentrated to the coast at depth. As anticipated from the density structure, maximum southward flow is found near the coast between 2200 and 3500 m. The inflow of almost 0.5 Sv that fills the deep Chile and Peru Basins is confined to within 500 km from the coast at 32.5°S, in agreement with P6E line deep water properties (potential temperatures less than 1.3°C were only observed east of 77°W). This inflow upwells within these basins and returns southward also within 500 km from the coast at 32.5°S. In the western Chile Basin, we find a weaker, deep northward flow of 3–4 Sv, concentrated on the eastern side of the East Pacific Rise. Taken together, these results show a
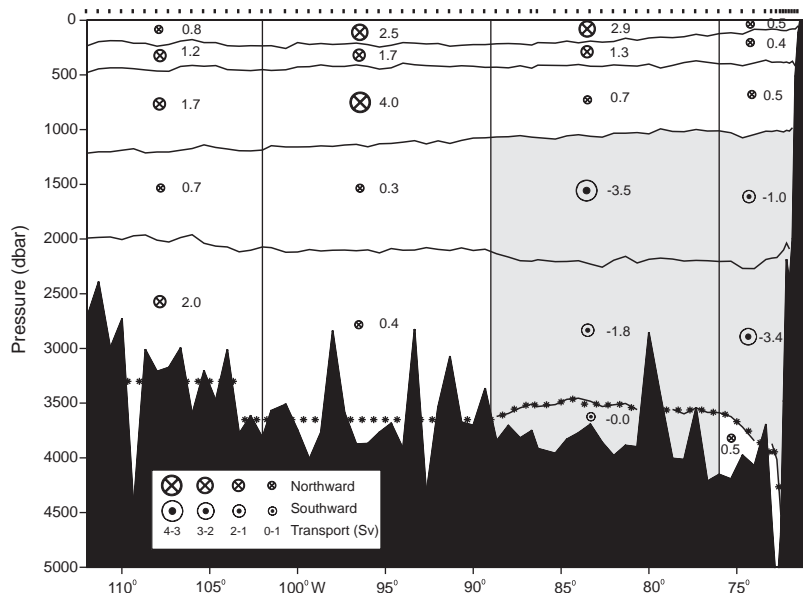
Fig. 6. North–south geostrophic transports (in Sverdrups) at 32.5°S in the Chile Basin, calculated from WOCE P6E section hydrographic data using estimated (see text) levels of no motion (asterisks). The density surfaces bounding the specific layers (see Table 4) were chosen from water mass properties in the region and the vertical box boundaries were chosen based on the zonal density structure at depth (see text). Southward transport is shaded. The positions of the WOCE hydrographic stations are indicated at the top of the figure.

net, deep poleward transport of 6–7 Sv of Pacific Deep Water at 32.5°S in the eastern South Pacific.

Our geostrophic transport calculations yield a total northward transport of 16–18 Sv within and above the main thermocline (our layers 1–3; above a potential temperature of about 3.5°C) at 32.5°S in the eastern South Pacific. Both the size and distribution of this upper ocean transport (i.e. greatest transport in the central part of the line) agree quite well with the mean Sverdrup transport along this line as estimated from mean satellite winds during the last decade (Fig. 7; from the same satellite wind data, integration of the meridional Ekman transport along this line yields 0.5 Sv to the north). It therefore may be useful to think of the mean circulation between the South American coast and the East Pacific Rise at 32.5°S as a combination of a relatively strong, equatorward, and mainly wind-driven, circulation in the main thermocline and a weaker, net poleward, and mainly thermohaline, circulation at depth (Figs. 6 and 7).

Our calculations show a total equatorward transport of SAMW/AAIW (layer 3) of about 7 Sv in the Chile Basin. This flow, which can be considered as part of both wind-driven and thermohaline circulations, is strongly concentrated in the western part of the Basin. In particular, well over half of the total estimated SAMW/AAIW transport along this line is found between 89°W and 102°W (Fig. 6). Such flow concentration is consistent with observed salinity and potential vorticity minima and oxygen maxima along the P6E line (Wijffels et al., 2001). Our current meter observations at 750 m depth within AAIW on the slope station showed a significant, 6-year mean, northward flow of 1.1 cm s^{-1} (and considerable interannual variability; Shaffer et al., 1999). This flow may be part of a narrow, boundary current on the slope and is probably not a major equatorward conduit of AAIW as proposed by Shaffer et al. (1995) based on limited data.

Our results also show weak, equatorward flow in the upper layers of the coastal section chosen for our analysis (Fig. 6). This also holds for the
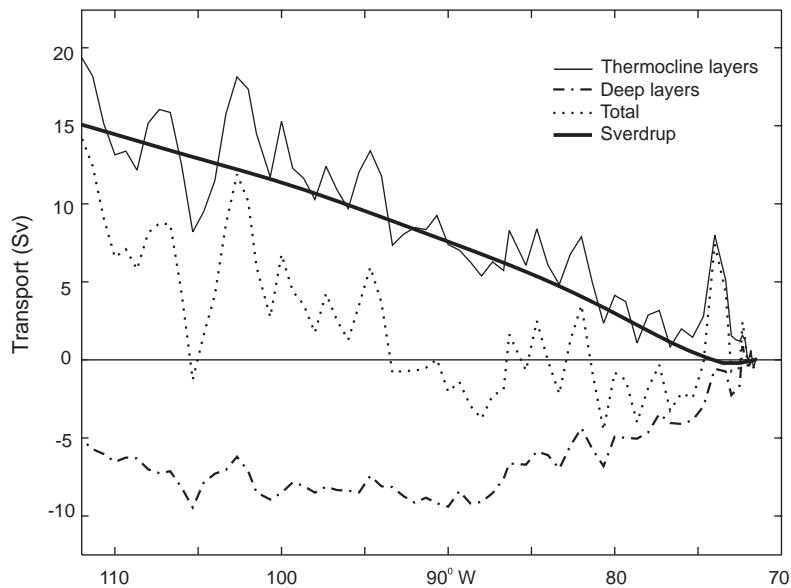
Fig. 7. Northward geostrophic transports integrated westward along the WOCE P6E line from the Chile coast using levels of no motion from Fig. 6. Shown are the total top to bottom transport (dotted line), the transport above the $\sigma_2 = 36.5$ density surface (top three layers in Fig. 6 and Table 4; solid line) and the transport below this surface (bottom three layers in Fig. 6 and Table 4; dashed-dotted line). Also shown is the northward Sverdrup transport integrated westward from the Chile coast at 32.5°S (thick line) as calculated from a 10 year mean of weekly winds from the ERS 1,2 satellite.

density range of the poleward, Peru–Chile Undercurrent (layer 2) in which a mean, equatorward flow of $0.3 \, \mathrm{cm \, s^{-1}}$ was calculated for the coastal section. Our slope station observations show strong, mean poleward flow of about $13 \, \mathrm{cm \, s^{-1}}$ in this density range and are consistent with an Undercurrent transport of about 1 Sv within about 50 km of the coast (Shaffer et al., 1997, 1999). Indeed, the density structure of the P6E line within this distance from the coast is consistent with a maximum in poleward flow there (Fig. 6). The observations from our deep ocean site show no significant mean flow in this density range about 150 km from the coast at 30°S but the salinity maximum and oxygen minimum, associated with Equatorial SubSurface Water carried poleward with the Undercurrent, can be traced at least 2000 km seaward of the coast in the P6E data (Wijffels et al., 2001). Thus, the true mean transport is probably southward in this density range, at least within our coastal section. Our calculated northward transport in the upper layers of this section probably reflects aliasing

due to strong current variability in this zone (Figs. 5 and 7).

5. Discussion

The low-frequency current variability observed at our deep ocean site off central Chile is considerably more complex than that observed at our nearby slope site, where such variability is controlled to a remarkable degree by remote forcing from the equatorial Pacific (Shaffer et al., 1997; Hormazabal et al., 2002). Rather, our deep ocean site is squarely embedded in an energetic, coastal transition zone, populated by eddies and filaments formed by baroclinic instability of the coastal current (Leth and Shaffer, 2001; Hormazabal et al., 2004). In addition, remotely forced Rossby waves "peel off" the coastal boundary and propagate westward past the deep sea site (Pizarro et al., 2002; Vega et al., 2003; Hormazabal et al., 2004). Our analysis of sea surface height anomalies and ADCP currents suggests that these waves,

joined by locally forced Rossby waves, are amplified as they approach the East Pacific Rise. The observed interannual modulation of low-frequency current variability at our deep sea site also differs greatly from that observed at the slope site. At the slope site, greater variability (periods <100 days) tends to accompany El Niño events. This variability reflects greater coastal trapped wave activity, ultimately forced by large wind fluctuations in the equatorial Pacific during the initial phase of El Niño events (Shaffer et al., 1999; Hormazabal et al., 2002). At the deep sea site, greater variability (periods >100 days) tends to accompany La Niña events. This variability may reflect greater available potential energy in the coastal current, more vigorous baroclinic stability, and more eddy generation during La Niña events (Hormazabal et al., 2004).

Deep southward flow off Chile was first identified based on hydrographic data from transpacific sections occupied during the SCOR-PIO expedition (Reid, 1973; Warren, 1973). Later Reid (1986) used geostrophic current calculations based on carefully chosen hydrographic stations to study the structure of the deep flow in the South Pacific. His analysis also highlighted an inter-mediate and deep poleward flow off Chile. The deep poleward flow was confirmed later by direct observations (Shaffer et al., 1995). A comparison of dissolved oxygen data from the SCORPIO cruises and a repeat of the SCORPIO sections in the eastern South Pacific in 1995 indicates that this flow may have intensified in recent decades (Shaffer et al., 2000).

Tsimplis et al. (1998) used hydrographic ob-servations along WOCE lines P6 and P21 (32°S and 17°S, respectively) in the context of inverse modeling to study the circulation of the South Pacific. In the results of their preferred solution (Model A, solution degree 30), poleward transport below the thermocline layers in the South Pacific (Pacific mid-depth outflow) was about 12 Sv, concentrated to the west of the East Pacific Rise (EPR). In this solution there was a net northward deep flow of several Sv east of the EPR with a deep poleward boundary current off Chile of about 6 Sv and a northward deep flow of about 8 Sv on the east flank of the EPR. Wijffels et al. (2001)

presented inverse calculations from P6 line data alone but with constraints from chosen mass and silica transports, prescribed Indonesian through-flow, and ALACE float data (Davis, 1998). Their preferred solution using the float data (Model A) exhibits a larger Pacific mid-depth outflow of about 20 Sv. They found a net poleward transport below the thermocline layers east of the EPR of about 14 Sv with a deep poleward boundary current off Chile of about 18 Sv and a northward deep flow of about 4 Sv on the east flank of the EPR. Sloyan and Rintoul (2001) presented inverse calculations for a high latitude, South Pacific box bounded to the north by the P6 line. They included independent diapycnal flux unknowns and air–sea flux constraints in their calculations and found an even greater Pacific mid-depth outflow of about 25 Sv. They determined a net poleward transport below the thermocline layers east of the EPR of about 16 Sv with a deep poleward boundary current off Chile of about 12 Sv and a southward deep flow of about 4 Sv on the east flank of the EPR.

This wide range of these results for the deep circulation in the Chile Basin reflects problems and uncertainties in the assumptions and methods used. For example, lower degree solutions of Tsimplis et al. showed strong, deep poleward flow throughout the Chile Basin. The method employed by these authors assumes mass and salt balance in a box formed by two trans-Pacific sections occupied two years apart. However, our deep current observations off Chile show significant changes in deep flow over such time scales. Indeed, the problem of non-synoptic observations in a varying flow field always haunts inverse box calculations (like those of Sloyan and Rintoul) based on the assumption of stationarity. The flow calculations of Wijffels et al, constrained by ALACE float data from 900 m depth, result in considerable zonal structure of near bottom flow in the western Chile Basin (and across the rest of the P6 line). Since near bottom, meridional flow in the western Chile Basin is region is probably constrained by local topography to be very weak (see above), this zonal structure may be an artifact and may reflect the difficulty of referencing very weak, deep ocean currents from limited-time

(albeit multi-year) observations in the main thermocline where currents are typically stronger and even more variable. Furthermore, the Wijffels et al. results show relatively strong poleward flow to the bottom off Chile. However, as discussed above, mean heat balance in the deep Chile and Peru Basins requires northward flow near the bottom there.

As opposed to the work cited above, our flow estimates for the eastern Chile Basin rest upon long-term, direct current observations and upon constraints arising from the heat balance in the deep Chile and Peru Basins. Therefore, our results are likely to be more robust for the eastern Chile Basin than the results cited above. We find a deep poleward boundary current off Chile of about 10 Sv that lies between low and high estimates discussed above and which is similar to the Sloyan and Rintoul estimate. On less firm ground, we estimated a deep northward flow on the eastern flank of the EPR of 3–4 Sv, which also lies between low and high estimates above and which agrees with the Wijffels et al. estimate. Taken together, our results paint a picture of weak, clockwise, deep circulation in the Chile Basin combined with a

stronger, deep poleward flow of 6–7 Sv entering this Basin from the north. From the above we conclude that a large portion of the Pacific mid-depth outflow takes place in a deep eastern boundary current off Chile.

The circulation scheme developed here is consistent with the distribution of $\Delta^{14}C$ along the WOCE 32°S line (Fig. 8). This shows a distinct wedge of the oldest water ($\Delta^{14}C < -220$ per mil) between 2000 and 3000 m depth within about 1000 km of the Chile coast. Water carried in this deep boundary flow apparently rounds the southern tip of South America and has been identified in the Drake Passage by its low salinity, low oxygen and high silicate properties (Naveira Garabato et al., 2002). Recently Well et al. (2003) used ^3He, hydrographic and ADCP data to trace the deep boundary flow off Chile through the Drake Passage and to estimate a net transport of this flow there to be 7 ± 1.2 Sv. A second subsurface minimum of $\Delta^{14}C$ in this depth range from 120°W to 180°W apparently marks a second main lobe of the Pacific mid-depth outflow. Higher $\Delta^{14}C$ values in this depth range are found on the eastern flank of the EPR, consistent with northward flow, as in
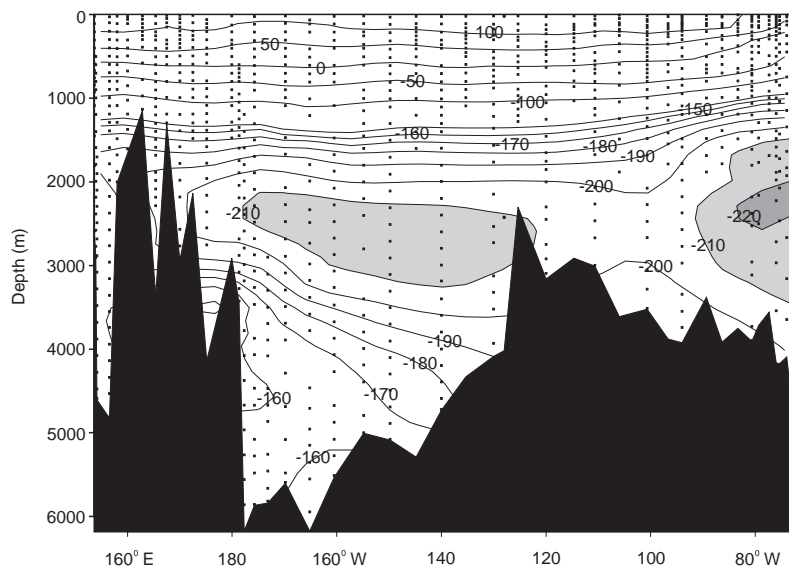

Fig. 8. The distribution of radiocarbon, expressed as $\Delta^{14}C$, along the transpacific WOCE P6 line at 32.5°S (based on a figure in Key (2001), Encyclopedia of Ocean Sciences; used with permission). Values below –210 and –220 per mil are lighter and darker shaded, respectively.

our results and in Tsimplis et al. and Wijffels et al. On the other hand, it is hard to reconcile the results of Sloyan and Rintoul with the observed Δ^{14}C distribution since their results show relatively strong northward flow between 130°W and 170°W and relatively strong southward flow between 100°W and 130°W in this depth range.

Simple ocean circulation theory (Stommel and Arons, 1960) predicts that any mid-depth outflow from the Pacific Ocean would be concentrated in a western boundary. However, direct current observations near the western boundary exhibit a deep inflow (of about 16 Sv), but not a mid-depth outflow (Whitworth III et al., 1999). On this basis, these authors concluded that the Pacific mid-depth outflow is likely to be much less than the deep inflow. Most other observational work, however, including the present analysis, supports a vigorous mid-depth outflow of about the same magnitude as the deep inflow (Fiadiero, 1982; Wunsch et al., 1983; Tsimplis et al., 1998; Wijffels et al., 2001; Sloyan and Rintoul, 2001). Tracer distributions (e.g. Fig. 8), combined with direct current observations and geostrophic calculations, indicate that the mid-depth outflow may be divided about equally between a broad flow west of the EPR and an eastern boundary current off Chile.

Our new observations and circulation calculations confirm and quantify a rather strong deep poleward, eastern boundary current off the west coast of South America, a flow that represents a significant branch in the deep circulation of the global ocean. One might ask whether such deep eastern boundary currents are the rule rather than the exception in the global ocean. Eby and Holloway (1994) reproduced such flows using a coarse-resolution, global ocean circulation model with a parameterization for the interaction of (unresolved) ocean eddies with bottom topography. However, recent simulations with the eddy-permitting, Parallel Ocean Program model ($\frac{1}{6}$ degree nominal resolution; forced by ECMWF-winds for the period 1985–1995) failed to reproduce a deep eastern boundary current off Chile, except for very weak poleward flow near the coast below about 3000 m (Ricardo Matano, personal communication). So it still is not known whether deep poleward eastern boundary currents are a ubiquitous feature of global ocean circulation and, if so, how such flows could be explained dynamically.

References

Davis, R., 1998. Preliminary results from directly measuring mid-depth circulation in the tropical and South Pacific. Journal of Geophysical Research 103, 24619–24640.

Eby, M., Holloway, G., 1994. Sensitivity of a large-scale ocean model to a parameterization of topographic stress. Journal of Physical Oceanography 24, 2577–2588.

Egbert, G.D., Ray, R.D., 2000. Significant dissipation of tidal energy in the deep ocean inferred from satellite altimeter data. Nature 405, 775–778.

Fiadiero, M.E., 1982. Three-dimensional modelling of tracers in the deep Pacific Ocean II. Radiocarbon and the circulation. Journal of Marine Research 40, 537–550.

Garrett, C., 2001. What is the near-inertial band and why is it different from the rest of the internal wave spectrum? Journal of Physical Oceanography 31, 962–971.

Hormazabal, S., Shaffer, G., Pizarro, O., 2002. Tropical Pacific control of intraseasonal oscillations off Chile by way of oceanic and atmospheric pathways. Geophysical Research Letters 29, 10.1029/2001GL013481.

Hormazabal, S., Shaffer, G., Leth, O., 2004. Coastal transition zone off Chile. Journal of Geophysical Research, 109, 10.1029/2003JC001596.

Key, R.M., 2001. Radiocarbon. In: Steele, J., Thorpe, S., Turekian, K. (Eds.), Encyclopedia of Ocean Sciences. Academic Press, London.

Leth, O., Shaffer, G., 2001. A numerical study of the seasonal variability in the circulation off Central Chile. Journal of Geophysical Research 106, 22229–22248.

Lonsdale, P., 1976. Abyssal circulation of the Southeastern Pacific and some geological implications. Journal of Geophysical Research 81, 1163–1176.

Morris, M.Y., Hall, M.M., St. Laurent, L.C., Hogg, N.G., 2001. Abyssal mixing in the Brazil Basin. Journal of Physical Oceanography 31, 3331–3348.

Naveira Garabato, A.C., Heywood, K.J., Stevens, D.P., 2002. Modification and pathways of Southern Ocean deep waters in the Scotia Sea. Deep-Sea Research Part I 49, 681–705.

Pizarro, O., Clarke, A.J., Van Gorder, S., 2001. El Niño sea level and currents along the South American coast: comparison of observations with theory. Journal of Physical Oceanography 31, 1891–1903.

Pizarro, O., Shaffer, G., Dewitte, B., Ramos, M., 2002. Dynamics of seasonal and interannual variability of the Peru–Chile Undercurrent. Geophysical Research Letters, 29, 10.1029/2002GL014790.

Pollack, H.N., Hurter, S.J., Johnson, J.R., 1993. Heat loss from the Earth's interior: analysis of the global data set. Reviews in Geophysics 31, 267–280.

Polzin, K.L., Toole, J.M., Ledwell, J.R., Schmidt, R.W., 1997. Spatial variability of turbulent mixing in the abyssal ocean. Science 276, 93–96.

Reid, J.L., 1973. Transpacific hydrographic sections at Lats. 43°S and 28°S: the SCORPIO expedition—III. Upper water and a note on southward flow at mid-depth. Deep-Sea Research 20, 39–49.

Reid, J.L., 1986. On the total geostrophic circulation of the South Pacific Ocean: flow patterns, tracers and transports. Progress in Oceanography 16, 1–62.

Reid, J.L., Mantyla, A.W., 1976. The effect of the geostrophic flow upon coastal sea elevation in the northern North Pacific Ocean. Journal of Geophysical Research 81, 3100–3110.

Shaffer, G., 1972. A theory of tme-dependent upwelling induced by a spatially- and temporally varying wind with emphasis on the effects of a seabreeze-landbreeze cycle. Kieler Meeresforschung 28, 139–161.

Shaffer, G., Salinas, S., Pizarro, O., Vega, A., Hormazabal, S., 1995. Currents in the deep ocean off Chile (30°S). Deep-Sea Research Part I 42, 425–436.

Shaffer, G., Pizarro, O., Djurfeldt, L., Salinas, S., Rutllant, J., 1997. Circulation and low-frequency variability near the Chile coast: remotely forced fluctuations during the 1991–1992 El Niño. Journal of Physical Oceanography 27, 217–235.

Shaffer, G., Hormazabal, S., Pizarro, O., Salinas, S., 1999. Seasonal and interannual variability of currents and temperature off central Chile. Journal of Geophysical Research 104, 29951–29961.

Shaffer, G., Leth, O., Ulloa, O., Bendtsen, J., Daneri, G., Dellarossa, V., Hormazabal, S., Sehlstedt, P.-I., 2000. Warming and circulation change in the eastern South Pacific Ocean. Geophysical Research Letters 27, 1247–1250.

Sloyan, B.M., Rintoul, S.R., 2001. The Southern Ocean limb of the global overturning circulation. Journal of Physical Oceanography 31, 143–173.

Stommel, H., Arons, A.B., 1960. On the abyssal circulation of the world ocean—II. An idealized model of circulation patterns and amplitude in oceanic basins. Deep-Sea Research 6, 217–233.

Tsuchiya, M., Talley, L.D., 1998. A Pacific hydrographic section at 88°W: water-property distribution. Journal of Geophysical Research 103, 12899–21918.

Tsimplis, M.N., Bacon, S., Bryden, H.L., 1998. The circulation of the subtropical South Pacific derived from hydrographic data. Journal of Geophysical Research 103, 21443–21468.

Vega, A., du Penhoat, Y., Dewitte B. , Pizarro, O., 2003. Equatorial forcing of interannual Rossby waves in the eastern South Pacific. Geophysical Research Letters, 30, 10.1029/2002GL015886.

Warren, B.A., 1973. Transpacific hydrographic sections at Lats. 43°S and 28°S: the SCORPIO expedition:—II. deep water. Deep-Sea Research 20, 9–38.

Well, R., Roether, W., Stevens, D., 2003. An additional deep water mass in Drake Passage as revealed by ^{3}He data. Deep-Sea Research Part I 50, 1079–1098.

Wijffels, S.E., Toole, J.M., Davis, R., 2001. Revisiting the South Pacific subtropical circulation: A synthesis of World Ocean Circulation Experiment observations along 32°S. Journal of Geophysical Research 106, 19481–19513.

Whitworth III, T., Warren, B.A., Nowlin Jr., W.D., Rutz, S.B., Pillsbury, R.D., Moore, M.I., 1999. On the deep western-boundary current in the Southwest Pacific Basin. Progress in Oceanography 43, 1–54.

Wunsch, C., Hu, D., Grant, B., 1983. Mass, heat, salt and nutrient fluxes in the South Pacific Ocean. Journal of Physical Oceanography 13, 725–753.